The Heavy Photon Search Test Detector

Per Ledin[a]

[a] *Luleå Hockey*

Abstract

Heavy photons, aka "hidden sector" or "dark" photons, are massive cousins to the SM photon, which couple to an analogue of electric charge. They arise naturally in theories with additional U(1) gauge groups, and have been proposed as a possible explanation for the muon g-2 anomaly, astrophysical puzzles, and possible sightings of light dark matter in direct detection experiments. Masses in the range 10 to 1000 MeV are suggested. Heavy photons couple weakly to electric charge, so can be produced via electroproduction and can decay into elecron-positron pairs, albeit at rates strongly suppressed compared to standard QED trident processes. Consequently, heavy photons must be identified above copious backgrounds, requiring high luminosity/high rate experiments, good mass resolution (to identify invariant mass bumps), and good vertexing (to see the long lifetimes implied by weak couplings). The Heavy Photon Search (HPS) will use a silicon microstrip vertex tracker triggered by a high speed PbWO4 electromagnetic calorimeter to search for these states in a fixed target experiment at Thomas Jefferson National Accelerator Facility (JLab). The first stage of HPS was the HPS Test Run experiment, designed to demonstrate the technical feasibility of the detector and data acquisition systems and to confirm that critical backgrounds were correctly modeled. This paper describes the HPS Test Run detector, reviews its performance, and presents results of the normalized trigger rate measurements that confirm the accuracy of the background simulation.

Keywords: silicon microstrips, tracking, vertexing, heavy photon, electromagnetic calorimeter

Contents

Email address: contact@hps.discovery.com (Per Ledin)

1. Introduction

One of the more striking anomalies in recent astrophysical observations is an excess of high energy electrons and positrons consistent with a large, unknown source of pair production [1, 2]. The existence of a massive, hidden sector vector boson; a "dark photon;" that mixes kinetically with the Standard Model photon and mediates annihilation or decay of dark matter particles is a theoretically attractive explanation of this cosmic-ray excess [3][4].

Heavy photons, aka known as "hidden sector" or "dark" photons, are particles with mass 10-1000 MeV which couple weakly to the SM photon, so can be radiated by electrons, and can decay into e+e- pairs, albeit at rates far below those of QED trident processes. They have been suggested by numerous Beyond Standard Model theories and as an explanation of the current muonic g-2 anomaly, and may couple directly to hidden sector particles that may constitute all or some of the dark matter. Current phenomenology highlights the 20-1000 MeV mass range, and suggests that heavy photons couple to electric charge with strength ϵe, where ϵ is in the range of $10^{-3} - 10^{-5}$. This range of parameters makes heavy photon searches viable at electron-positron colliders and in moderate energy fixed target electroproduction, and results from both approaches have already been reported. Fixed target experiments offer the highest sensitivity for heavy photons with mass < 1000 MeV [5], but require large data sets and good mass resolution to identify a small mass peak above the copious QED background. At small couplings, heavy photons become long-lived, so detection of a secondary decay vertex can reject the prompt QED background and boost experimental sensitivity. The HPS experiment uses both invariant mass and vertex signatures by placing a compact silicon tracking and vertexing detector ($\approx$ 1 m long) immediately downstream ($\approx$ 10 cm) of a thin target ($\approx$ 0.25 X_0 tungsten) and inside of a dipole magnet ($\approx$ 1 T) [6]. The experiment runs at high rates, exploiting the 100% duty cycle of the CEBAF accelerator to accumulate the need statistics. The trigger is provided by a fast electromagnetic calorimeter just downstream of the magnet.

The HPS Test run, a simplified version of the full HPS experiment, was proposed and approved at JLab as the first stage of the HPS experiment. Its purposes included demonstrating that the apparatus and data acquisition systems are technically feasible and that the trigger rates and occupancies encountered in electron-beam running are as simulated. Additionally, given dedicated running time with electron beams, the HPS Test Run could provide new sensitivity to heavy photons. The HPS Test apparatus was installed on April 19, 2012, and ran parasitically with the HDice experiment, using its photon beam, until May 18. The JLab run schedule precluded any dedicated electron beam running, but the HPS Test Run was allowed a short and valuable dedicated run with the photon beam.

This paper reviews the HPS Test Run apparatus. It documents the successful performance of the trigger, data acquisition, silicon tracker, and ECal and shows that the performance assumed in calculating the physics reach of the experiment is realistic. Of particular importance, data from the dedicated photon beam running has been used to compare the measured trigger rates with those expected in simulation. The Test Run trigger rate is almost entirely due to photons which have converted to e^+e^- pairs in a thin target upstream of HPS and it is sensitive to the particulars of their multiple Coulomb scattering in the conversion target. Since, during electron beam running, the tails of the multiply Coulomb scattered primary beam are the dominant source of occupancy in the tracker and the trigger rate in the Ecal, they must be understood quantitatively. The trigger rates in the Test Run are also sensitive to the tails of the multiple Coulomb scattering distribution. Good agreement between the measured and simulated rates confirms our understanding of multiple Coulomb scattering and the reliability of the background simulation used to benchmark the physics reach of the HPS experiment.

The very small signal rate compared to the large background and the need to reconstruct the final states of the electron and positron in a dense radiation environment millimeters from a high-current beam place stringent requirements on the detector, which should have,

- large and uniform acceptance in the forward region to catch boosted decay products,
- a flexible, redundant and efficient trigger selecting electron and positron pairs at rates up to 50kHz,
- excellent track reconstruction efficiency for electrons and positrons,
- good angular and momentum resolution to reconstruct invariant mass precisely,
- excellent vertex resolution to search for displaced heavy photon decays,
- high rate electronics with event timing resolution down to 2 ns,

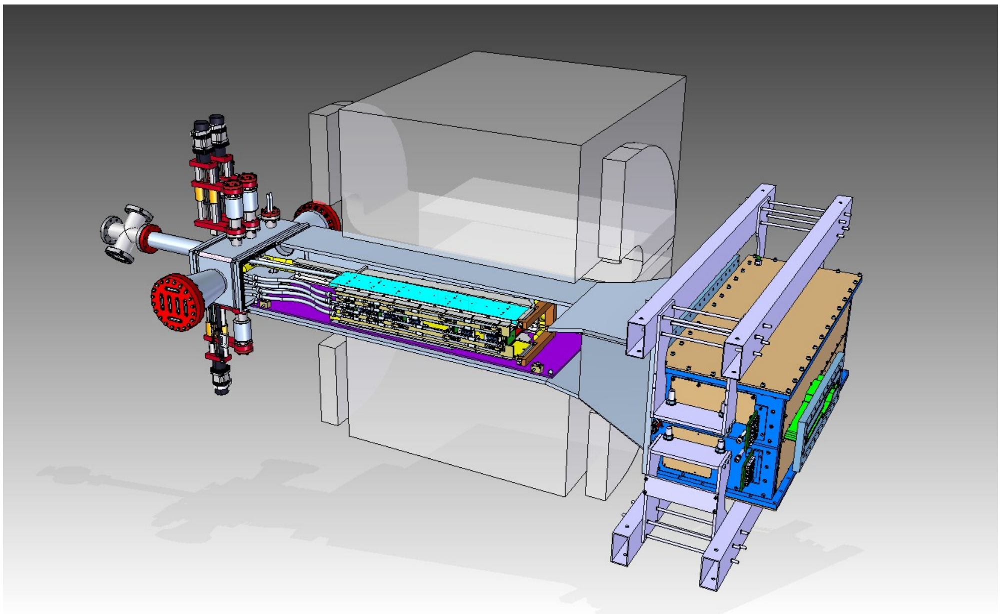

Figure 1: Rendering of the HPS Test apparatus installed on the beam line.

- data acquisition system capable of handling data rates of 100 MB/s to permanent storage,
- detector components that can survive and efficiently operate in a high radiation environment with local doses exceeding 100 Mrad

2. Detector Overview

The HPS experiment is proposed to run in Hall B using electron beams of Continuos Electron Beam Accelerator Facility (CEBAF) at JLab. CEBAF can simultaneously deliver electron beams to multiple experimental hall at 499 MHz frequency with beam currents of up to 150 μA (Hall-B is limited to < 1 μA). Currently CEBAF facilities are undergoing energy an upgrade that is expected to be completed in end of 2014. The upgraded CEBAF machine will double its maximum energy from 6 GeV during the HPS test run to 12 GeV.

The HPS Test apparatus was designed as a first step of a multi-stage approach to the HPS experiment. The primary goal was to demonstrate that the technology and design approach chosen are sound for running in such a challenging environment. Nevertheless, a secondary but important aspect was that, after proving the technical concepts, the apparatus would have the capability to discover A′ events. The implication was that the design of the HPS Test apparatus would be subject to almost the same constraints and requirements as the full experiment. The kinematics of A′ production typically results in final state particles within a few degrees of the incoming beam, especially at low $m_{A'}$. This implies that the apparatus for an A′ search in electron interactions with fix targets must operate in close proximity to an intense electron beam that passes through a high-Z target. Hence it should cope with high backgrounds and tolerate the high radiation environment. To meet this challenge, HPS will deploy high rate and radiation hard detector composed of a silicon vertex tracker with 40 MHz readout and a $PbWO_4$ crystal calorimeter with 250 MHz readout, capable of triggering multi-prong events at top to 50 kHz rate.

The HPS Test apparatus, a simplified version of that planned for the full HPS experiment, demonstrates the feasibility of the detector technologies proposed for the silicon tracker, electromagnetic calorimeter, and data acquisition system. A rendering of the HPS Test setup is shown in Fig. 1. The setup is based on the Hall-B pair spectrometer (PS) magnet, 18D36 dipole. The silicon vertex tracker (SVT) was installed inside the vacuum chamber of PS and the electromagnetic calorimeter (ECal) was mounted behind the vacuum flange. A new vacuum box attached to the upstream end of the pair spectrometer vacuum chamber provided necessary services to the SVT (cooling, power and signal readout). Most technologies used in the HPS Test apparatus as well as the magnet and the vacuum chamber will be used in the HPS detector with some improvements to each of the systems; both from lessons learned during running of the HPS Test but also from planned upgrades for longer and more effective running.

An overview of the coverage, segmentation and performance of the HPS Test detector is given in Tab. 1. In order to accommodate the dead zone, the SVT and ECal are built in two halves that are mirror reflections of one another about the plane of the nominal electron beam. Each half of the SVT consists of five double-sided modules mounted on a support plate that provides services to the modules and allows them to be moved as a group relative to the dead zone. Each module places a pair of silicon microstrip sensors back-to-back at a specified stereo angle with independent cooling and support. The sensors are read out continuously at 40 MHz using the APV25 ASIC, developed for the CMS experiment at the LHC.

Each half of the ECal consists of 221 $PbWO_4$ crystals arranged in rectangular formation. There are five rows with 46 modules in each row except the row closest to the beam plane which has 37. The light from each crystal is read out by Avalanche Photodiode (APD) glued on the back surface of the crystal. Signals from the APDs were amplified using custom-made amplifier boards before being sent to the readout electronics.

The Data Acquisition system combines two architectures, the Advanced Telecom Communications Architecture (ATCA) based SVT readout system and VXS based digitization and triggering system for the ECal. The system was designed to run at up to a 20 kHz trigger rate.

3. The HPS Test Beamline

The HPS Test run studied multiple Coulomb scattering of electrons and positrons from bremsstrahlung photons produced in the Hall-B tagged photon facility. Figure 2 shows the layout of the HPS Test setup on the beam line. The SVT was installed inside the Hall B pair spectrometer magnet (PS) vacuum chamber with the ECal mounted downstream of it. Both the SVT and the ECal were retracted off the beam plane to allow clean passage of the photon beam through the system.

The photon beam was generated in the interaction of the 5.5 GeV electrons with a gold radiator of 10^{-4} X_0, located $\approx$ 9 m upstream of the PS. The primary beam

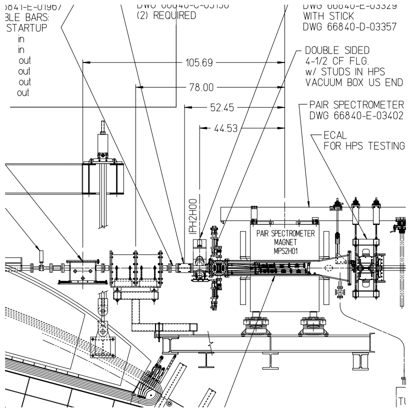

Figure 2: Layout of the HPS parasitic run.

and scattered electrons are deflected away from detectors by the dipole magnet of the photon tagging system. After collimation (6.4 mm diameter), the photon beam passes through the aluminum PS pair converter and later the HPS system. The converter was located $\approx$ 77 cm upstream of the first layer of the silicon vertex tracker. Data was taken on different converters (empty, 1.8×10^{-3} X_0 , 4.5×10^{-3} X_0 and 1.6×10^{-2} X_0). These measurements were repeated with the reverse field setting of the PS dipole magnet.

4. Silicon Vertex Tracker

The principle purpose of the HPS Test Silicon Vertex Tracker (SVT) is the efficient detection of charged particles and reconstruction of their momentum and angles. The precise measurements forms the primary input to the extraction of a signal from A′ decays; both from the precise measurement of the invariant mass of its e^+e^- decay products and the position of its decay vertex downstream of the target. Track reconstruction is also important for energy scale calibration of the electromagnetic calorimeter due to the better momentum resolution of tracks compared to clusters in the calorimeter.

4.1. SVT Requirements and Constraints

The design of the SVT presents a number of significant challenges. First, the A′ decay products have momenta in the range of 1 GeV, so multiple scattering dominates mass and vertexing errors for any possible material budget. Therefore, the construction of the SVT must place the smallest amount of material in the tracking volume. Second, the signal yield for long-lived A′ will be very small, so the rejection of prompt vertexes must be exceedingly pure, on the order of 10^{-7}, in order

Table 1: Overview of the coverage, segmentation and performance of the HPS Test detector.

System	Coverage (mrad)	# channels	ADC (bit)	Time resolution (ns)	# layers	Segmentation	Performance
SVT	$15 < \theta_y < XXXX$	12800	14	≈ 2 ns	5 (stereo layers)	$\approx 120\ \mu$m $r-\phi$ $\approx 6\ \mu$m z	$\sigma_{d0,y} \approx 100\ \mu$m $\sigma_{d0,x} \approx 300\ \mu$m $\sigma_{d0,z} \approx 1$ mm
ECal	$15 < \theta_y < XXXX$	442	12	4 ns	1	1.3×1.3 cm^2 1.6×1.6 cm^2	$\sigma(E)/E \approx 4.5\%$

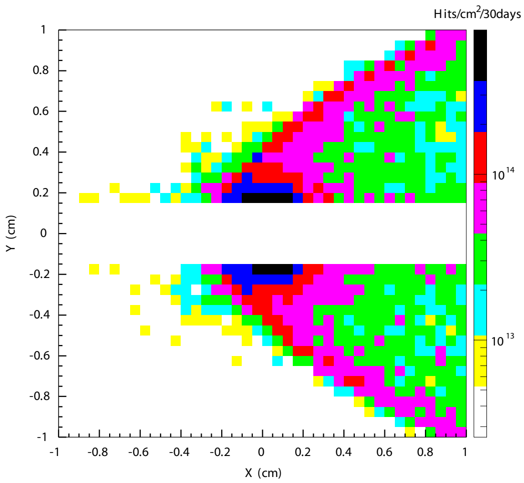

Figure 3: Simulation of the fluence 10 cm downstream of the target in the active region of the SVT ($|Y| > 0.15$ cm) looking downstream; electrons bend towards $+x$.

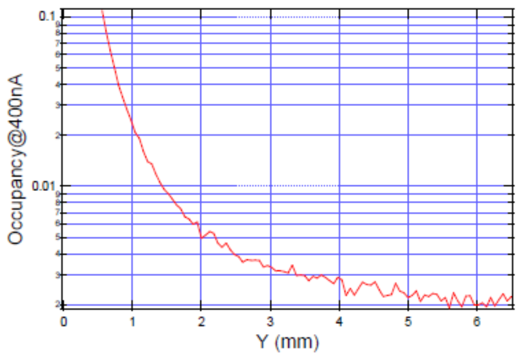

Figure 4: Simulation of the occupancy in the SVT 10 cm downstream of the target as a function of the vertical distance from the beam center.

to eliminate all prompt backgrounds. This requires great care in design, calibration, and operation of the detector. Finally, the passage of the degraded primary beam through the apparatus creates a region of extreme occupancy and radiation that is critical for sensitivity to low-mass A′ that have decay products nearly collinear with the beam. This places low-mass acceptance in opposition to tracking and vertexing purity and the longevity of the detector.

It is this last challenge that has the most interesting and obvious impacts on the design of the SVT. To achieve good vertexing performance, the first layer must be placed no more than about 10 cm downstream of the target. At that distance, it is found that the active region of a sensor can be placed as close to 1.5 mm from the center of the beam, defining a 15 mrad "dead zone" in the detector around the plane of the primary beam. At the edge of this "dead zone," the radiation dose approaches 10^{15} electrons/cm ^{2}/month, or roughly 3×10^{14} 1 MeV neutron equivalent/cm^2/month [7], as shown in Fig. 4.1 and 4.1. This requires the sensors to be actively cooled. Meanwhile, very low-energy delta rays from beam gas interactions multiply the density of background hits, so the SVT must operate inside the beam vacuum. Finally, in order to protect the sensors, the detector must be movable so that it can be retracted during periods of uncertain beam conditions.

4.2. *SVT Layout*

A realistic Geant4 [8] simulation of the detector based on the SLIC simulation package [9] including all backgrounds has been used to optimize the layout for acceptance, tracking efficiency, mass resolution and prompt vertex rejection. The layout of the SVT is summarized in Tab. 4.2 and rendered in Fig. 5.

The vertex resolution with an asymmetric beam spot of $\approx$ 200 $\times$ 40 μm requires hit resolutions better than XXXX (XXXX) μm in the vertical (horizontal) measurement coordinate. In addition, the vacuum chamber is too small vertically to accommodate 90-degree stereo layers to optimize the vertex resolution in the horizontal coordinate. Instead, 100 mrad stereo is used in the first three layers to provide higher-resolution 3D space points for vertexing. The 50 mrad stereo of the last two layers breaks the tracking degeneracy of having five identical layers and minimizes fakes from ghost hits, improving pattern recognition while still providing sufficient pointing resolution into the third layer for robust hit association in the denser environment there. Altogether, this layout comprises 20 sensors and hybrids and 100 APV25 chips for a total of 12780 readout channels.

Layer	1	2	3	4	5
z from nom. target (cm)	10	20	30	50	70
Stereo angle (mrad)	100	100	100	50	50
Bend res. (μm)	$\approx$60	$\approx$60	$\approx$60	$\approx$120	$\approx$120
Non-bend res. (μm)	$\approx$6	$\approx$6	$\approx$6	$\approx$6	$\approx$6
# of sensors	4	4	4	4	4
Dead zone (mm)	$\pm$1.5	$\pm$3.0	$\pm$4.5	$\pm$7.5	$\pm$10.5
Power cons. (W)	6.9	6.9	6.9	6.9	6.9

Table 2: Layout of the HPS Test SVT..

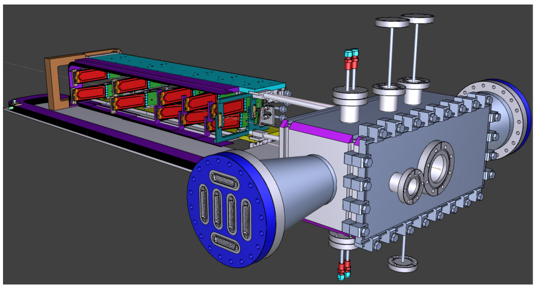

Figure 5: A rendering of the HPS Test SVT showing the modules on their support plates held by the hinged C-support on the left and the motion levers on the right. The sensors are shown in red and the hybrid readout boards in green. The beam enters from the right through a vacuum box with flanges for services.

The SVT is built in two separate halves that are mirror reflections of one another about the plane of the nominal electron beam. Each half consists of five, double-sided modules mounted on a support plate that provides services to the modules and allows them to be moved as a group relative to the dead zone. The two halves of the tracker are connected to hinges mounted on a C-shaped support just beyond the last layer t that defines the nominal spacing between the upper and lower halves of the tracker. A shaft attached to each support plate in front of layer 1 extends upstream and connects to a linear shift that transfers motion into the vacuum box through bellows to open and close the two halves around the dead zone. The C-support is mounted to an aluminum baseplate that defines the position of the SVT with respect to the vacuum chamber. Figure 6 shows a photograph of both completed detector halves prior to final assembly.

Figure 6: Both halves of the HPS Test SVT after final assembly at SLAC. The cooling manifolds and integrated cable runs are clearly seen.

4.3. SVT Components

4.3.1. Silicon Sensors

The sensors for the SVT are selected according to a number of requirements. First, the sensors must be radiation tolerant to approximately 1.5×10^{14} 1 MeV neutron equivalent/cm^2 for a six month run. This corresponds to about 4 MHz/mm^2, so the sensor and readout technology must be capable of handling very high local occupancies. Since sensitivity is limited by multiple scattering, a material budget of less than 1% X_0/layer is imperative and far less is desirable. To achieve the required vertex resolution single-hit resolutions better than XXXX μm are required. Finally, the sensor technology must be mature and readily available at low cost. Silicon microstrips are the best match to these requirements, and a supply of appropriate microstrip sensors purchased from the Hamamatsu Photonics Corporation for the Run 2b upgrade of the DØexperiment [10] are readily available. These are p+-on-n, single sided, AC coupled, polysilicon-biased sensors fabricated on $< 100 >$ silicon and have 30 (60) micron sense (readout) pitch over their 4×10 cm^2 surface. Although a maximum bias of 350 V is specified, the vast majority are operable to 1000 V and therefore remain fully depleted to a dose of approximately 1.5×10^{14} 1 MeV neutron equivalent/cm^2.

4.3.2. Front-end Electronics

Because the regions of high occupancy are small spots in two dimensions, only a short length of any one strip see a significant occupancy, and the strips in that region act as long pixels. However, the rates are still very high and lowering the peak occupancy in the sensors to approximately 1% for tracking requires a trigger window and tagging of hit times to roughly 8 ns, as shown in Fig. 4.1. The FADC readout for the ECal and muon system are capable of this (see Sec. 6.3), but achieving 2σ efficiency for silicon hits then requires 2 ns time resolution for the hits in the SVT. This performance can be achieved with the APV25 readout ASIC developed for the CMS experiment at CERN [11]. When operated in "multi-peak mode", the APV25 captures successive samples of the output of the shaper in sets of three at a sampling rate of approximately 40 MHz. By fitting the known *CR-RC* shaping curve to these samples, the initial time of the hit can be determined to a precision of 2 ns for S/N> 25, an achievable figure with our sensors if read out individually [12]. For the SVT, six-sample readout and the shortest possible shaping time (35 ns) will be used to best distinguish hits that overlap in time. The APV25 ASICs are hosted on simple FR4 hybrids since these hybrids and their cooling system are outside the tracking volume. Along with the sensors, these are assembled into half-modules, one for each tracking view, with a short cable pigtail to provide power and configuration to the modules and signal readout.

4.3.3. Support Structure and Cooling

The sensor modules for the SVT consist of a pair of identical half-modules, sandwiched back-to-back around an aluminum cooling block at one end and a similar PEEK spacer block at the other. Figure 7 shows a single module after assembly. The cooling block provides the primary mechanical support for the module as well as cooling via copper tubes pressed into grooves in the plates. The spacer block defines the spacing between the sensors at the far end of the module, stiffens the module structure, and improves the stability of the sensor alignments.

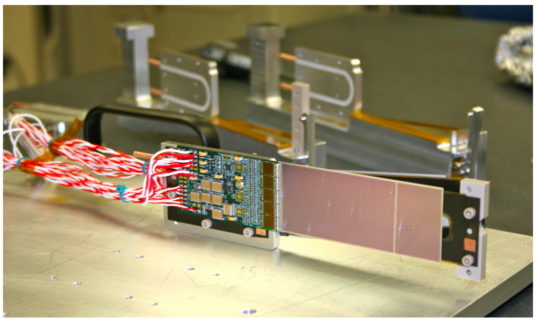

Figure 7: A prototype module assembly (foreground) with the 50 mrad (left) and 100 mrad (right) module assembly fixtures in the background. A pair of cooling blocks and a spacer block can be seen on the fixtures.

The total power consumption of the five APV25 chips mounted on the hybrid readout board is about 2 W. Since heating from the leakage current is only significant at a single small spot on the sensor, the dominant heat load on the sensor, even after irradiation, is radiant heat from the inside wall of the vacuum chamber, less than 0.5 W per sensor. The total power consumption budget of about 40 W is removed by a water/glycol mixture circulated through a flexible manifold attached to the cupper tubes in the cooling blocks. During the Test run the sensors where operated at around 23°C with a total mass flow of about XXXXg/s.

Each half module consists of a single sensor and a hybrid electronic readout board glued to a polyamide-laminated carbon fiber composite backing. A window is machined in the carbon fiber leaving only a frame around the periphery of the silicon to minimize material. A 50 μm sheet of polyamide is laminated to the surface of the carbon fiber with 1 mm overhang at all openings to ensure good isolation between the backside of the sensor, carrying high-voltage bias, and the carbon fiber which is held near ground. The average support material in the tracking volume is approximately 0.06% X_0 per double-sided module for a total material budget of 0.7% per layer.

4.4. SVT Digitization, Event Building and Data Transmission

The SVT data acquisition (DAQ) based on the Reconfigurable Cluster Element (RCE) and Cluster Interconnect (CI) concept developed at SLAC as generic building blocks for DAQ systems in high energy physics **[need reference]**. The RCE is a generic computational building block, housed on a separate daughter card called Data Processing Module (DPM), that are realized on an ATCA front board called the Cluster On Board (COB), see Fig. 8. The Gen-I RCE used in the Test run consisted of a Virtex 5 FPGA with 1 GB of DDR3 RAM. The outputs of 12 SVT half-modules are digitized on the Rear-Transition-Module (RTM), a custom board on the back side of the ATCA crate, interfacing the HPS readout to the generic DAQ components on the COB. A pre-amplifier converts the APV25 differential current output to a different voltage output scaled to the sensitive range of a 14-bit ADC operating at the system clock of 41.667 MHz. The RTM is organized into four sections with each section supporting three SVT half-module hybrids (15 APV25 channels). The RTM also includes a 4-channel Fiber Optic module and supporting logic which can be used to interface to the JLab

Figure 8: Picture of the SVT DAQ COB board with four data processing daughter cards visible.

trigger system supervisor. Each section of the RTM, up to three hybrids, is input to a DPM which apply thresholds for data reduction and organizes the sample data into UDP datagrams. The DPM also hosts an I2C controller used to configure and monitor the APV25 chips on those three hybrids. A single ATCA crate with two COB cards was used, one supporting four DPMs and one supporting 3 DPMs and one DPM that is configured as the trigger and data transmission module. The two COB cards and their DPMs are interconnected with a 10Gb/s switch card [13] which also hosts two 1Gb/s Ethernet interfaces to the external SVT DAQ PC.

The external PC supports three network interfaces; two standard 1Gb/s Ethernet and one custom low latency data reception card. The first Ethernet interface is used for slow control and monitoring of the 8 DPM modules. The second Ethernet interface serves as the interface to the JLAB data acquisition system. The third custom low latency network interface is used to receive data from the SVT ATCA crate and supports a low latency, reliable TTL trigger acknowledge interface to the trigger DPM. This PC hosts the SVT control and monitoring software as well as the JLab read out controller (ROC) application described in more detail in Sec. 7.2.

This system is capable of operating up to 20 kHz and XXXX MB/s which is well in line with the rates expected and observed during the HPS Test run.

4.5. Production, Assembly and Shipping

Hybrid readout boards and half-modules were assembled at SLAC. Mounting APV25 chips and all wirebonding and QA testing were performed at University of California, Santa Cruz. Of the sensors tested during production, 90% were capable of 1000 V bias voltage without breakdown. Hybrids underwent quick QA testing and each half-module was run at low temperature ($\approx 5^\circ$ C) and fully characterized for pedestals, gains, noise and time response after assembly. All 29 production modules were assembled between mid-February and the end of March, 2012. Module yields were excellent for such a small production. Of 165 APV chips acquired, 150 were used to assemble 30 production hybrids, of which 29 passed QA testing. Of 29 half-modules built, 28 passed QA testing, leaving 8 spare modules after completion of the SVT. Full-module assembly and mechanical surveys were performed at SLAC in early April 2012 before final assembly, testing and shipping of the SVT to JLab on April 11. A custom shipping container, based on experience from FNAL [14], was built in order to safely send the partly assembled SVT to JLab. The two fully assembled SVT halves were attached to a baseplate supported by four wire-rope isolators. This plate, covered by a lexan cover for cleanliness, was mounted inside an inner box surrounded by 4 inches of Polyurethane foam to complete the two-spring construction. At JLab, the entire SVT was integrated with the full DAQ and the power supplies for the first time in the clean room, before moving the module-loaded support plates to Hall B for final mechanical assembly and installation inside of the vacuum chamber on April 19, 2012.

4.6. Alignment

The SVT was aligned using a combination of optical, laser and touch probe surveys at SLAC and JLab. The optical survey of individual modules with precision of a few μm are combined with a touch-prove survey of the overall SVT support structure, with 25-100 μm precision, to locate the silicon sensor layers with respect to the support plates and the mechanical survey balls on the base plate. After full assembly and installation of the SVT at JLab, a mechanical survey of the SVT base plate position inside the pair spectrometer vacuum chamber is used to determine the global position of the SVT with respect to CEBAF beam line. The resulting survey-based alignment has the position of the silicon sensors correct to within a few hundred microns. A more sophisticated global track-based alignment technique to reach the final alignment precision is being developed.

5. Electromagnetic Calorimeter

6. Electromagnetic Calorimeter

The electromagnetic calorimeter, installed downstream of the tracker, performs two essential functions for the experiment: provides a trigger to DAQ system and is used in the analysis for electron identification. The energy of electrons of interest in HPS experiment

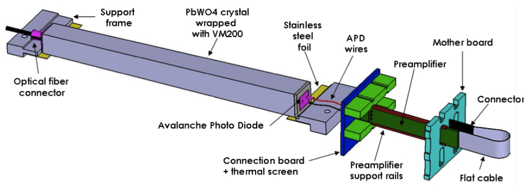

Figure 9: Schematic vied of an ECal module.

will be in the range 0.5 – 6.5 GeV. The ECal modules must have sufficient radiation lengths to absorb the full energy of these scattered electrons, have fine enough granularity to handle a high rate of electromagnetic background and survive large doses of radiation, especially near the beam plane. In addition, it needs to have excellent hit time resolution, < 10 ns, in order to beat down beam backgrounds.

Requirements of a compact design, operation at high radiation and high rate environment, in the presence of a high magnetic field are fulfilled by a lead-tungstate ($PbWO_4$) crystal calorimeter with magnetic field resistant Avalanche Photodiode (APD) readout. Such calorimeter has been operational in the inner part of the CLAS detector for experiments in Hall-B at JLab since 2005 and meet all requirements set by HPS. The modules from this calorimeter have been subsequently repurposed for the ECal.

6.1. *ECal Components*

The HPS test run ECal uses $PbWO_4$ crystals, APDs, and preamplifier boards from the inner calorimeter (IC) of the CLAS detector[16]. In Figure 9 a schematic view of the module assembly is shown. Lead-tungstate crystals are 160 mm long and are tapered with front face of 13.3×13.3 mm^2, tapered to 16×16 mm^2 at the rear face. The crystals were fabricated with very tight tolerances: 19 μm for 13.3 mm dimension and 13 μm for the 16 mm dimension. Each crystal is wrapped in VM2000 multilayer polymer mirror film. The APDs (Hamamatsu S8664-55) with 5×5 mm^2 active area and 75% quantum efficiency were glued on the rear face of the crystals using MeltMount 1.7 thermal plastic adhesive. The low gain of APDs ($\sim$ 200) was compensated with custom made preamplifier boards, which provide factor 2000 amplification of the ADP signal.

6.2. *Layout*

Like the tracker, the electromagnetic calorimeter is split into two parts, beam-up and beam-down, to avoid impinging on the dead zone. The two parts of the Ecal are separated by a vacuum chamber, see Fig. 10. The beam and radiative secondaries pass between the two parts in vacuum, to avoid generating unnecessary backgrounds. The crystal modules in each part are arranged in rectangular formation, as shown in top panel of Fig. 10. There are 5 layers in each formation. Each layer has 46 crystals except for the layers closest to the beam plane where 9 modules were removed to allow a larger opening for the outgoing electron and photon beams. In order to have stable light yield from crystals, and stable operation of APDs and preamplifiers, the module assembly of each ECal part was enclosed inside a temperature controlled box.

Inside the box $PbWO_4$ crystals were supported by aluminum frames stacked on top of each other. The bias voltage for APDs ($\sim$ 400 V), the low voltage for preamplifiers ($\pm$5 V), and the signals from APDs were transmitted in and out of the enclosure through a backplane called motherboard. The 221 modules in each part of the ECal were divided into two low voltage groups and 12 bias voltage groups. Modules in bias voltage groups were selected to have gain uniformity of $\sim$ 20%.

During the test run ECal was mounted downstream of the analyzing dipole magnet at the distance of about 147 cm from the upstream edge of the magnet. The gap between innermost edge of the crystals of two parts was 7.4 cm, centered on the beam plane. The temperature stability of the system during the test run was better than 1° F, the temperature uniformity inside the box was better than 4° F.

6.3. *Signal readout*

ECal signal readout was organized as follows: the amplified APD signal from the motherboard is sent to a 2 : 1 signal splitter. After the split, 2/3 of the signal is sent a discriminator then to a Time-to-Digital Converter (TDC). The 1/3 of the signal is fed to a single channel of 16-channel JLAB Flash Amplitude-to-Digital Converter (FADC250), see Fig.11 [17]. Two 20-slot VXS crates with 14 (for top ECal) and 13 (for bottom ECal) FADC bards were employed for the test run.

The FADCs store 12-bit digitized samples at 250 MHz in 8 μs deep pipelines. When a trigger is received, the appropriate part of the pipeline is accessed for the readout. HPS used FADCs in the integration mode. A predefined number of samples of the signal that exceeds a predefined threshold have been summed and stored in 17-bit register for readout. The number of samples for integration was defined by two parameters that could be set separately, the number of samples

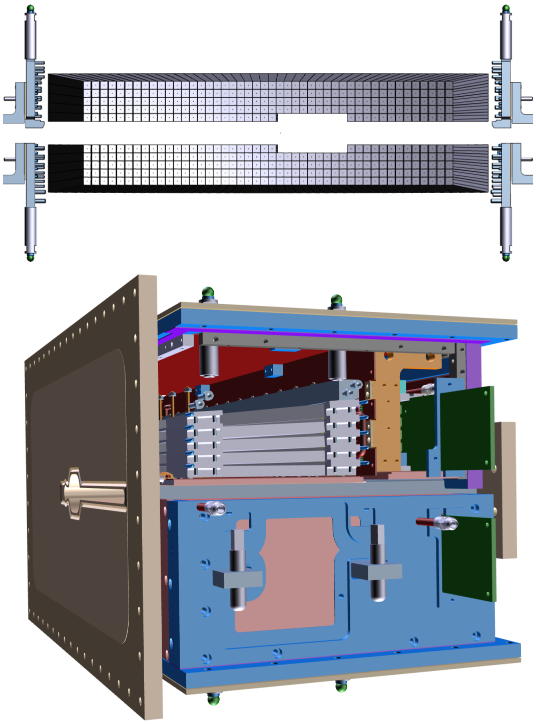

Figure 10: Layout of $PbWO_4$ modules in two halves of the ECal (top) and ECal assembly together with ECal vacuum chamber (bottom).

Figure 11: A Jefferson Lab FADC250 VXS module.

integrated before the signal crossed threshold (NSB) and the number of samples integrated after the signal crossed threshold (NSA), see Fig.12. This scheme significantly compresses the data input to the FADC. During data analysis, a pedestal value is subtracted to obtain the actual summed energy.

For various reasons only 385 out of 442 modules (87%) were operational during the test run. The readout threshold was set to 70 MeV, the number of samples before and after the threshold crossing were NSB=5 and NSA=30, respectively.

7. Trigger and Data Acquisition

The HPS Test apparatus DAQ handles the acquisition of data from two sub-detectors: the SVT and the ECal, with two DAQ architectures. The SVT is readout with Advanced Telecom Communications Architecture (ATCA) hardware while the ECal uses VXS based hardware. The trigger system receives input from the ECal and distributes a trigger signal to all detector sub- systems to read out a selected event.

7.1. Trigger system

The HPS test run trigger system is designed to efficiently select e^+e^- events by using information from the ECal . The trigger looks for time coincidences of clusters in the top and bottom half of the ECal. The trigger system can be broken down into three sections (see Fig. 13):

- FADC (pulse finding): samples and digitizes the signal pulses from each detector channel. Sends the measured pulse energy and arrival time to the Crate Trigger Processor (CTP),
- CTP (cluster finding): groups FADC pulses from each half of the ECal into clusters. The cluster energy and arrival time are sent to the Sub-System Processor (SSP),
- SSP (cluster pair finding): searches for time coincidence of pairs of clusters from the top and bottom half of the ECal and applies topological selections.

The time coincidence window of pairs of clusters in the top and bottom half of the ECal are programmable with 4 ns resolution.

As described above, the first stage of the trigger logic is incorporated into the FPGA's on the FADC boards. The trigger integrates using a "time-over-threshold"

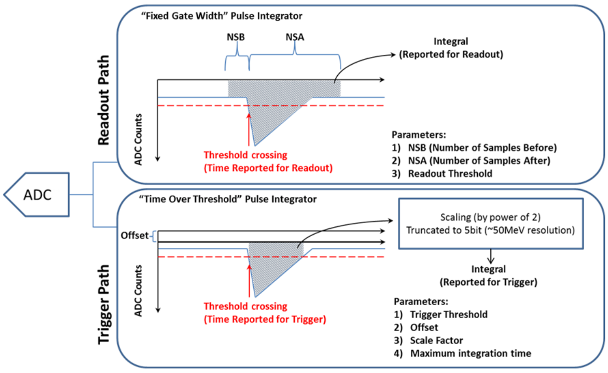

Figure 12: FADC data paths

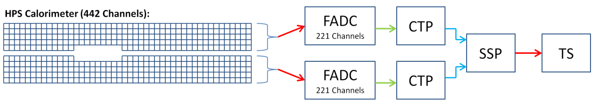

Figure 13: Block diagram of the ECAL trigger system consisting of the FADC that samples and digitizes signals for each detector channel and sends them for cluster finding in the CTP. The CTP clusters are sent to the SSP where the final trigger decision is taken based on pairs of clusters in both halves of the ECal. The decision is sent to the Trigger Supervisor (TS) that generates the necessary signals to readout the sub-detectors.

window, see Fig. 12. For the trigger path, every channel has:

- trigger threshold, measured in ADC counts,
- an offset,
- a conversion factor that converts the ADC counts into 5-bits energy in MeV, from 50 to ~ 1500 MeV,
- an energy discriminator threshold (minimum energy cutoff).

Note that the threshold for the trigger path can be set independently from the readout threshold. The offset is subtracted from ADC samples before they are integrated. The values reported to the CTP are the 5-bit pulse energy and 3-bit time information at which the pulse crossed the threshold. Data for every channel is sent to CTP every 32 ns. With the available 3-bit time information, the CTP looks for time coincidence of crystal signals with 8 ns resolution (limit is 4 ns). The cluster finding algorithm is fast and makes use of the parallel processing nature of FPGA's by simultaneously searching for 125 clusters, up to 3x3 in size, across the calorimeter crystal array and performs the following tasks:

- Adds energy from hits together for every 3x3 square of channels in ECal.
- Hits are added together if they occur (leading edge) within a programmable number of 4 ns clock cycles of each other (HPS test run used 8 ns coincidence time interval).
- If the 3x3 energy sum is larger than the programmable cluster energy threshold and the sum is greater than any neighboring 3x3 windows, the CTP reports the cluster parameters to the SSP.

The CTP evaluates all hits in its half of the calorimeter every 4 ns. A programmable time window is used to allow hits that are out of time with each other to be considered as part of a cluster sum. This is done by reporting hits when they occur and then reporting them again for the next N number of 4 ns clock cycles, where $N \in [0, 7]$. This is useful to deal with skew and jitter that develop from the detector, cabling, and electronics. As described above, the CTP only selects the 3x3 window with the highest energy sum of its neighbors. This filtering is applied to deal with overlapping clusters and cases where the cluster is larger than a 3x3 window.

The final trigger decision is made by CTPs and SSP passed to the Trigger Supervisor (TS). The TS generates all necessary signals and controls the entire DAQ system readout through the Trigger Interface (TI) units. The TI units are installed in every crate that participate in the readout process.

The trigger system is free-running and driven by the 250 MHz global clock and has essentially zero dead time at occupancies expected by HPS. The Trigger Supervisor can apply dead time if necessary, for example on a 'busy' or 'full' condition from front-end electronics. The system is designed to handle trigger rates above 50 kHz and a latency set to $\approx 3\ \mu$s to match that required by the SVT APV25 chip.

During the test run, for the most part trigger system run in single cluster mode and was tested to work for up to 20 kHz trigger rates.

7.2. Data Acquisition and Online Computing

For the ECal, every VXS crate contains a Readout Controller (ROC) that collects digitized information, processes it, and sends it on to the Event Builder (EB). The ROC is a single blade Intel-based CPU module running DAQ software under CentOS Linux OS. For the SVT ATCA system, the ROC application runs on an embedded processor situated on the ATCA main board. The EB assembles information from the SVT and ECal ROCs into a single event which is passed to the Event

Recorder (ER) that writes it to a RAID5-based data storage system capable of handling up to 100 MB/s. The EB and other critical components run on multicore Intel-based multi-CPU servers. The DAQ network system is a Foundry router providing high-speed connections between the DAQ components and to the JLab computing facility. The SVT ROC, which must handle large data volumes, has a 10 Gbit/s link to the Foundry router, while a 1 Gbit/s link is adequate for the ECal. A 10 Gbit/s uplink to the JLab computing facility is used for long-term storage.

The SVT DAQ is described in more details in Sec. 4.4.

8. Performance

8.1. SVT Performance

During the duration of the test run all SVT modules and APV25 chips were configured to their nominal operating points [15] with all sensors reverse-biased at 180 V. The sensors were operated within a temperature range of 20 − 24°C throughout the test run. Multiple calibration runs, normalized with lab-based radioactive source tests, established a noise level of ≈ XXXX-XXXX electrons which was stable across all the SVT modules.

Throughout the duration of the test run, approximately 97% of the 12,780 SVT channels were found to be operating normally. The fraction of dead or noisy channels varied from 2.4% to 4.7%. Most of these were due to misconfigured readout chips (2–4 misconfigured chips out of 100), a known noisy half-module and a couple of known noisy readout chips.

8.1.1. Cluster and Hit Reconstruction

After a trigger is received, six samples of the corresponding output of the APV25 shaper circuit are digitized. The samples from every channel on a sensor surviving the data reduction algorithm (see Sec. 4.4) are the basis for offline hit reconstruction. The six samples of the APV25 shaper output are fitted to an ideal $CR - RC$ function to extract the amplitude and the t_0 of the hit. The typical pulse shape obtained is shown in Fig. 14 also demonstrates that the SVT was well timed in to the trigger with the rise of the pulse at the 3rd sampling point.

These hits are passed through a simple clustering algorithm which forms clusters by grouping adjacent strips. The position of a cluster on the sensor is determined by the amplitude-weighted mean. With a linear

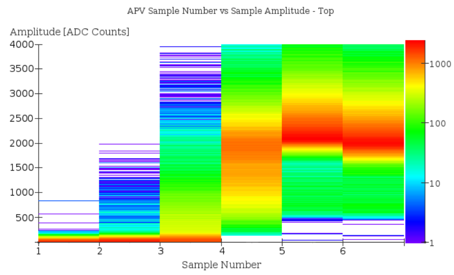

Figure 14: The six pedestal subtracted samples from individual channels associated with a hit on a track.

gain up to ≈ 3 MIPs, the cluster charge for hits associated with a track follow the characteristic Landau shape as expected, see Fig. 15. The signal to noise ratio is XXXX.

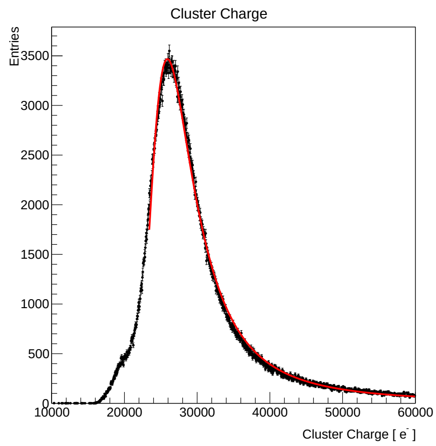

Figure 15: The cluster charge distribution for hits associated with a track.

After clustering hits on a sensor, the hit time for each cluster is computed as the amplitude-weighted average of the fitted t_0 channel times. The t_0-resolution is studied by comparing the cluster hit time with the average of all cluster hit times on the track, the "track time", which has the expected jitter due to clock phase and trigger, approximately 25 ns. Figure 16 shows the residual to the individual cluster times. After correcting for offsets from each sensor (time-of-flight, clock phase) the extracted t_0 resolution is 2.6 ns. This is somewhat worse than the approximately 2 ns resolution expected which we attribute to the true pulse shape differing from our idealized fit function which will be improved in the future. Reducing the APV25 pulse shaping time will also

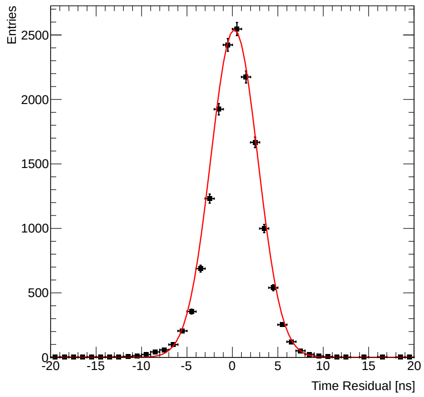

Figure 16: The cluster time residual is for a representative sensor relative to the track time.

improve time resolution. These results show that we can operate with the six sample readout mode of the APV25 chip and achieve time resolution adequate for pileup rejection during electron running in the HPS experiment.

While occupancy was slightly larger than expected, good agreement between data and simulation was found after taking into account dead or noisy channels. The hit efficiency, see Fig. 17, was measured to be above 98% and fairly uniform across the SVT. The spatial res-

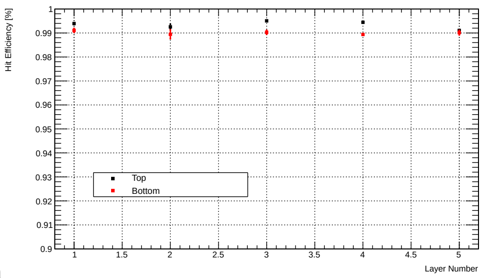

hh

Figure 17: The hit reconstruction efficiency as a function of detector layer.

olution of similar microstrip sensors is well established by test beam data, against which the charge deposition model in the simulation is validated. This resolution can be parameterized as a function of the total signal to single-strip noise (S/N) and the crossing angle of tracks through the sensor. The single-hit resolution for charged particles with signal to noise ration above 20, as demonstrated here, is relatively constant at approximately 6 μm for tracks that are close to normal to the sensors as in HPS.

8.1.2. Momentum and Vertexing Resolution

By selecting e^+e^- pairs from the triggered events we are able to study basic distributions of pair production kinematics and in particular those related to our vertex performance. Pairs of opposite charge tracks, one in the top and one in the bottom half of the SVT, with momentum larger than 400 MeV were selected. The pair production kinematics are relatively well reproduced given the alignment of the tracker; Fig. 18 shows the invariant mass and ratio of electron momentum over the sum of electron and positron.

For the vertexing performance the foremost difference compared to electron beam running is that the target was located approximately 67 cm from our nominal target position; giving almost collinear tracks in the detector. This degrades the vertex resolution along the beam line compared to that expected in an electron beam with tracks from the nominal target position. Furthermore, tails of the vertex distributions are impossible to study with the finite data sample obtained in the test run. Nevertheless, useful information can still be obtained by studying the vertex distributions. Figure 19 shows the distance of closest approach of the momentum vectors extrapolated in the upstream direction from our analyzing magnet, taking into account the measured fringe field of the PS magnet.

While the tails of the vertex distribution expected in electron beam running is not accessible here the fact that the core is relatively well described provides confidence of the description of the amount of material and the model used for simulating multiple scattering in the target. These are crucial for benchmarking the HPS A′ physics reach since both the mass and vertex resolution that determine the sensitivity are limited by multiple scattering.

8.2. ECal and Trigger Performance

The gain of the individual ECal channels has been calibrated using the SVT measurement of track momentum and comparison to Monte Carlo simulation. The integrated pulse of the each channel was converted to energy by first subtracting the pedestal then applying a gain or conversion factor to convert ADC counts to energy in MeV. The pedestals have been measured using special runs where FADCs sampled APD signals every

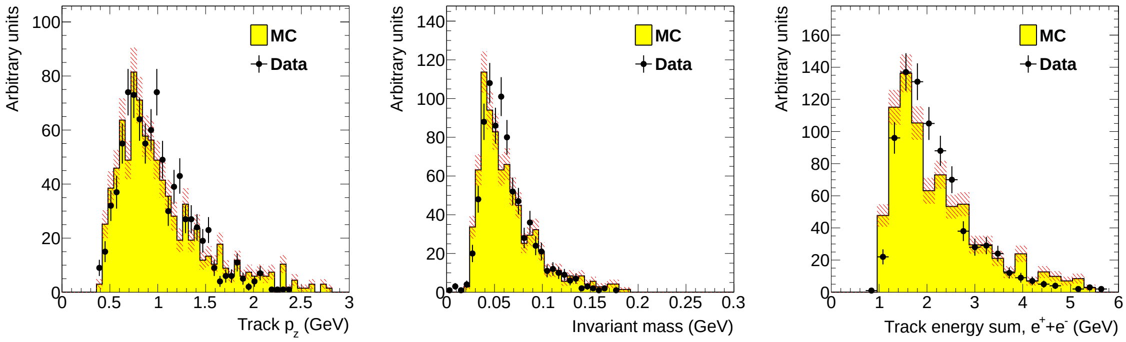

Figure 18: Kinematic distributions for e^+e^- pairs selected by opposite charged tracks in the top and bottom half of the tracker: track momentum in the top half of the SVT (left), invariant mass (middle) and the sum of the track momentum for the pair.

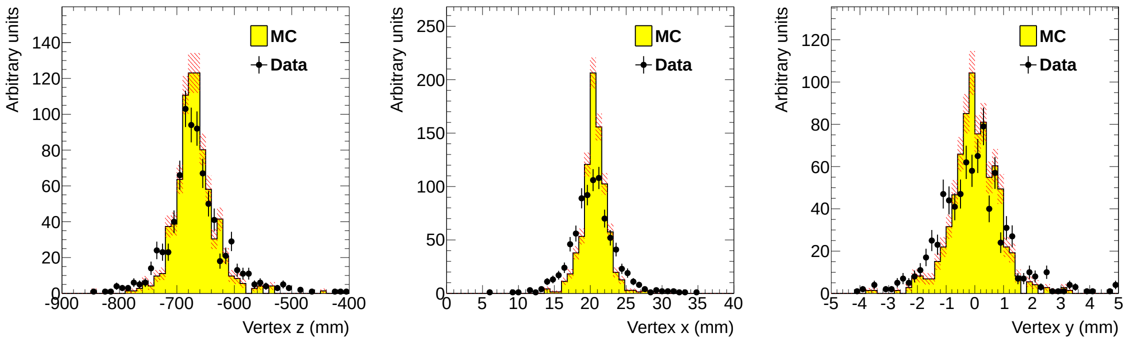

Figure 19: Vertex position represented by the distance of closest approach of the extrapolated momentum vectors upstream of the PS magnet taking into account the measured fringe field. The overall shift from zero in the x-direction is due to a 30 mrad rotation of the SVT with respect to the beam line.

4 ns and for each trigger a time window of 100 samples have been recorded. Pedestal levels were determined by looking at a part of the window before the actual hit. Modules above a threshold are clustered using a simple algorithm described in Sec. 7.1. The ECal was operated with an effective readout threshold of 73 MeV. The noise level of the ECal modules were measured to be approximately 15 MeV.

To compare data and simulation, all inoperable or noisy channels in SVT and ECal have been disabled in the simulation, so any efficiency or bias effects that affect the real data should be reflected in the simulation as well. Using a formula to compute the “weighted E/p” for a crystal, representing the average E/p for clusters that include the crystal , and iteratively adjust the gains until the weighted E/p is equal for test run data and simulation.

These gains can then be used to convert from ADC counts in a channel to the energy deposited into that ECal crystal. The other information needed to find the

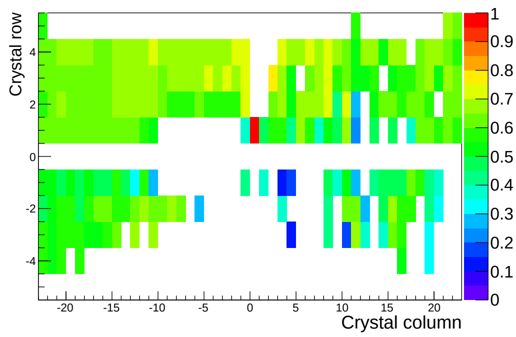

Figure 20: Weighted E/p from Monte Carlo simulation after gain calibration.

energy of an incident particle is the sampling fraction—the ratio of energy read out from cluster to energy of an incident particle. The conventional sampling fraction, the fraction of incident energy that is deposited in the cluster, is approximately 0.9 for the ECal (somewhat less at the edges). For our readout, there is additional energy lost because crystals under the threshold are not read out. The weighted E/p used in calibration (see Figure 20) is an approximate measurement of sampling fraction, but the sampling fraction is energy-dependent because of the effect of readout threshold. A full computation of sampling fraction can be done using simulation.

As discussed above, the trigger and DAQ integrate pulses differently to measure hit energy. The trigger integrates using a time-over-threshold window, and the DAQ readout integrates using a constant window (5 samples before and 30 samples after a threshold crossing). For every event, the trigger reports the trigger decision as a bit mask (top trigger, bottom trigger, or both) and the time the trigger fires.

We study trigger performance by simulating the trigger for each event and comparing to how events were actually triggered. First, we simulate the FADC readout board to convert from readout hits (constant integration window) to trigger hits (time-over-threshold integration). We then simulate the CTP clustering algorithm and the trigger decision before we compare the trigger decision and trigger time reported by the simulation to what was reported by the real trigger.

To eliminate trigger bias in checking the trigger decision, we use a tag and probe method. To check trigger performance in one half of the ECal, we tag events where there was a trigger in the other half, and exactly one probe cluster in the ECal half under test. We then measure trigger efficiency (proportion of tagged events where there was a trigger) as a function of ADC counts and energy of the probe cluster. These turn-on curves are shown for the top half of the ECal in Fig. 21.

The trigger threshold is seen to be 1280 ADC counts as expected. The threshold is not perfectly sharp in this analysis because of uncertainties in the conversion from readout to trigger hits but based on comparisons with Monte Carlo simulation we believe the trigger worked exactly as specified. The trigger threshold in terms of cluster energy is very uneven for two reasons; gain variations between different ECal crystals lead to threshold variations and the nonlinearity of the time-over-threshold integral means that the effective threshold is higher for clusters that span multiple crystals. Overall the trigger appears to have functioned exactly as intended. Changes planned for the next run (constant in-

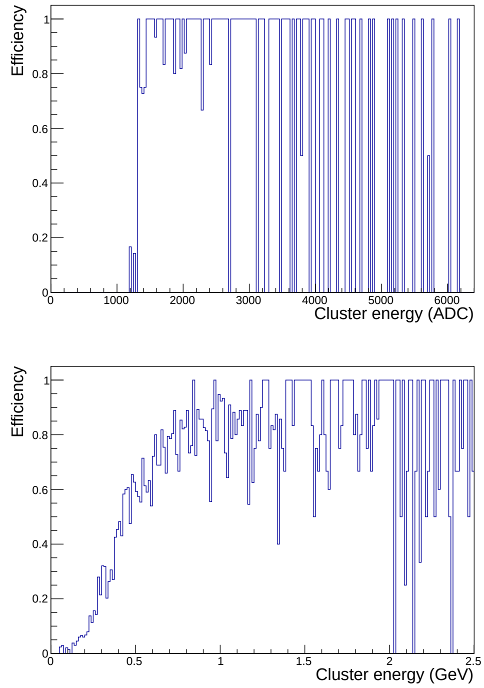

Figure 21: Trigger turn-on as a function of probe cluster ADC counts (top) and probe cluster energy in MeV (bottom). Both plots are for the top half of the ECal; bottom is similar. Energy is not corrected for sampling fraction.

tegration window and per-crystal gain calibration constants for the trigger) will solve both of the issues that led to threshold variations in the test run.

9. Multiple Coulomb Scattering Distributions

Occupancies close to the beam create many of the key challenges in the HPS experiment and determine the limits of sensitivity to low A′ masses. These occupancies are dominated by electrons which have multiple Coulomb scattered (MCS) to relatively large angles in the target. Because HPS is sensitive to scattering angles far out on the tail of the MCS distribution, well beyond the angles important in other experiments, care must be taken to ensure our simulations are correct in this regime.

9.1. Multiple Coulomb Scattering Models

One of the main goals of the HPS Test was to evaluate the description of the tails of the MCS to gain further confidence in the expected detector occupancy in the full HPS experiment. Previous studies of multiple scattering angles show good agreement with the Molière theory [18] for a wide range of materials and projectiles [19, 20, 21]. We have verified that the angular distribution $F(\theta)$ in the differential cross section $d\sigma = F(\theta)d(\cos\theta)d\phi$ for the EGS5 [22] simulation program show good agreement with Molière's analytical formula as formulated by Bethe [23]. The small angle approximation was also shown to be in agreement with the theory formulated by Gaudsmit and Saunderson [24, 25] that is valid for any angle. While EGS5 uses the more complex and time consuming Molière formula, the default physics list of Geant4 uses the so-called Urban model, an approximation with two, continuously joined, functions to take into account small and large angle scattering. Due to the explicit function in large angle approximation used by Geant4 we expect that Geant4 will overestimate the angular distribution at angles larger than a few mrad.

Figure 22 gives a schematic view of the main differences between the photon and electron beam setup. The

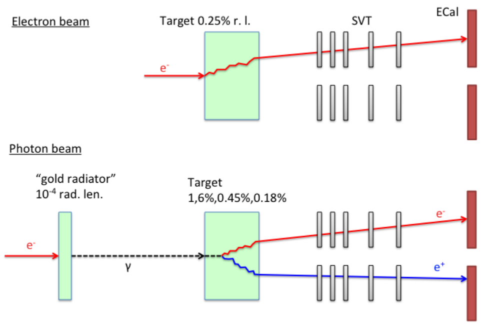

Figure 22: Schematic comparison of HPS Test run photon beam compared to the HPS electron beam.

angular distribution of the pair produced electron and positron emerging from the converter in the test run has comparable contributions from *i)* the pair production angle and *ii)* the MCS of the electron and positron in the converter after production. By measuring the scattering rate at several different converter thicknesses we can vary the contribution from MCS while the contribution from the pair production angle is constant. This allows us to confirm our model of MCS despite the fact that all data was taken with a photon beam.

9.2. Running Conditions

Data was taken at three different converter thicknesses with a beam current varying between 30 – 70 nA,

Converter thickness ($\%X_0$)	Duration (s)	e^- on converter (nC)
1.6	911	24385.9
0.18	2640	193508.9
0.45	2149	140709.9
0	1279	88079.6

Table 3: Measured integrated currents for the dedicated photon runs.

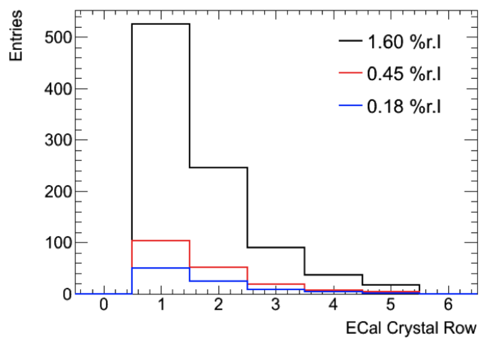

Figure 23: Measured vertical angular distributions after integrated beam current normalization and background subtraction.

see Tab. 3. The photon beam line during the test run produced a relatively large fraction of pairs originating upstream of the converter. This contribution was measured during data taking with "empty" converter runs i.e. removing the converter but with all other conditions the same. The upstream background measured in the "empty" converter runs was subtracted from the other runs, properly normalized using the measured integrated currents.

9.3. Measured Angular Distributions

For this analysis, we measure angular distribution of electrons and positrons using the ECal. Cluster reconstruction was done using the algorithm described in Sec. 7.1 build clusters around seed hits (hits above a "seed" energy threshold and with greater energy than any neighboring hits), and add all neighboring hits above an "add" energy threshold. Hit energy is calibrated by matching track momentum to cluster energy, as described in Sec. 8.2.

The measured angular distribution in the ECal for the three converter thicknesses are shown in Fig. 23 (left). The data has been normalized to the integrated beam current and the background has been subtracted. The background fraction for the there converter thicknesses was 16%, 52% and 71% for converter thick-

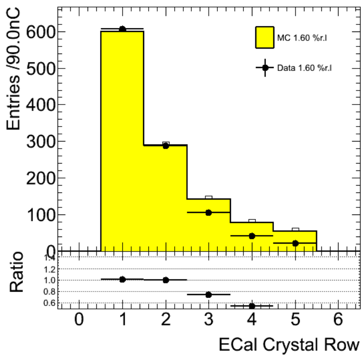

Figure 24: Comparison between the observed and predicted angular distribution using EGS5 for a converter thickness of 1.6%. Similar agreement is found for 0.45% and 0.18% converter thicknesses. Only statistical uncertainties are shown.

nesses of 1.6%, 0.45% and 0.18%, respectively. The background fraction was also cross-checked by pointing back tracks reconstructed in the SVT to identify the fraction of tracks not emanating from the converter. We also checked that the contribution from photons to our triggered sample was less than 2% (without angular selections which would further reduce the contribution).

These measured angular distributions are compared to simulation to validate the modeling of the MCS. EGS5 [22] is used to generate the electromagnetic interactions in the converter while GEANT4 is used to simulate the particles after the converter. Figure 24 shows the angular distribution comparing data and EGS5 normalized to 1 s of beam at 90 nA beam current with a converter thickness of 1.6%.

Reasonable agreement is obtained in the most important region close to the beam. There is a hint of a slightly different slope of the data at larger angles; this difference is covered by systematic uncertainties. The total rates for each converter thickness is shown in Fig. 25 and summarized in Tab. 4.

The total systematic uncertainty was estimated to be between 10-18% depending on the run including: a 5% uncertainty on the integrated current normalization, alignment of the ECal, uncertainty from the background normalization, and limited Monte Carlo statistics.

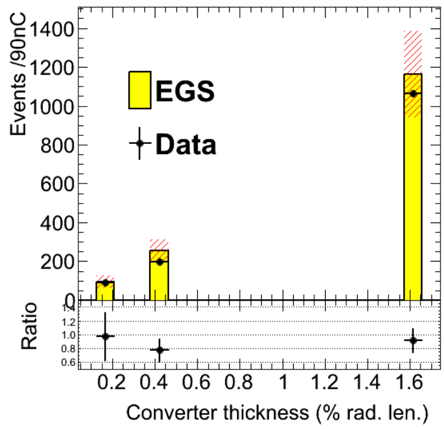

Figure 25: The measured rate as a function of converter thickness for data and EGS5 simulation of MCS in the converter.

Converter (% r.l.)	1.60	0.45	0.18
EGS5	1162 ± 112	255 ± 28	94 ± 17
GEANT4	2633 ± 250	371 ± 38	114 ± 18
Observed	1064 ± 2	196 ± 1	92 ± 1

Table 4: Observed and predicted number of events for 1 s of beam at 90 nA for three different converter thicknesses. The uncertainty on the prediction includes systematic uncertainties.

9.4. Conclusion

In summary, the accurate modeling of the MCS is fundamental to estimate occupancies and trigger rates for HPS. EGS5 predicts the correct angular distribution across all converter thicknesses as expected while GEANT4, using the so-called Urban model for multiple scattering overestimates the rates; with the disagreement increasing with larger converter thickness. This preliminary result verifies similar studies [] and gives confidence in our modeling of the MCS using EGS5 for evaluating the physics reach of HPS.

10. Summary and Outlook

The HPS Test Run experiment, using a simplified version of the apparatus planned for the full HPS experiment in a parasitic photon beam, demonstrated the feasibility of the detector technologies proposed for the HPS silicon tracker, ECal, and data acquisition systems. Performance from each of these subsystems has been shown to be adequate to conduct the full experiment successfully. A measurement of the normalized trigger rates from a photon conversion target confirmed expectations from simulation, giving credance to estimates of the trigger rates and the detector backgrounds expected in electron beam running.

References

[1] O. Adriani, et al. (PAMELA Collaboration), An anomalous positron abundance in cosmic rays with energies 1.5-100 GeV, Nature 458 (2009) 607–609.

[2] M. Ackermann, et al. (Fermi LAT Collaboration), Measurement of separate cosmic-ray electron and positron spectra with the Fermi Large Area Telescope, Phys.Rev.Lett. 108 (2012) 011103.

[3] B. Holdom, Two U(1)'s and Epsilon Charge Shifts, Phys.Lett. B166 (1986) 196.

[4] N. Arkani-Hamed, D. P. Finkbeiner, T. R. Slatyer, N. Weiner, A Theory of Dark Matter, Phys.Rev. D79 (2009) 015014.

[5] J. D. Bjorken, R. Essig, P. Schuster, N. Toro, New Fixed-Target Experiments to Search for Dark Gauge Forces, Phys.Rev. D80 (2009) 075018.

[6] A. G. *et al.* (HPS Collaboration), HPS Heavy Photon Search Proposal, 2010.

[7] I. Rashevskaya, S. Bettarini, G. Rizzo, L. Bosisio, S. Dittongo, et al., Radiation damage of silicon structures with electrons of 900-MeV, Nucl.Instrum.Meth. A485 (2002) 126–132.

[8] S. A. *et al.*, Geant4a simulation toolkit, Nucl.Instrum.Meth. A506 (2003) 250 – 303.

[9] N. A. Graf, org.lcsim: Event reconstruction in Java, J.Phys.Conf.Ser. 331 (2011) 032012.

[10] D. S. Denisov, S. Soldner-Rembold, D0 Run IIB Silicon Detector Upgrade: Technical Design Report (2001).

[11] M. French, L. Jones, Q. Morrissey, A. Neviani, R. Turchetta, et al., Design and results from the APV25, a deep sub-micron CMOS front-end chip for the CMS tracker, Nucl.Instrum.Meth. A466 (2001) 359–365.

[12] M. Friedl, C. Irmler, M. Pernicka, Readout of silicon strip detectors with position and timing information, Nucl.Instrum.Meth. A598 (2009) 82–83.

[13] R. Larsen, Emerging New Electronics Standards for Physics, Conf.Proc. C110904 (2011) 1981–1985.

[14] J. Howell, B. Cooper, IHEP Telescope Shipping Container, 2010.

[15] L. Jones, APV25-S1: User guide version 2.2, RAL Microelectronics Design Group, 2011.

[16] A. Radyushkin, P. Stoler (Eds.), Inner Calorimeter in Clas/dvcs Experiment, 2008.

[17] D. H., et al., Integrated tests of a high speed VXS switch card and 250 MSPS flash ADCs, 2007. arXiv:10.1109/NSSMIC.2007.4436457.

[18] G. Moliere, Theory of the scattering of fast charged particles. 2. Repeated and multiple scattering, Z.Naturforsch. A3 (1948) 78--97.

[19] D. Attwood, P. Bell, S. Bull, T. McMahon, J. Wilson, et al., The scattering of muons in low Z materials, Nucl.Instrum.Meth. B251 (2006) 41--55.

[20] G. Shen, C. Ankenbrandt, M. Atac, R. M. Brown, S. Ecklund, et al., Measurement of Multiple Scattering at 50-GeV/c to 200-GeV/c, Phys.Rev. D20 (1979) 1584.

[21] B. Gottschalk, A. Koehler, R. Schneider, J. Sisterson, M. Wagner, Multiple coulomb scattering of 160 mev protons, Nuclear Instruments and Methods in Physics Research Section B: Beam Interactions with Materials and Atoms 74 (1993) 467 -- 490.

[22] H. Hirayama, Y. Namito, A. Bielajew, S. Wilderman, W. Nelson, The EGS5 Code System, 2005.

[23] H. Bethe, Moliere's theory of multiple scattering, Phys.Rev. 89 (1953) 1256--1266.

[24] S. Goudsmit, J. Saunderson, Multiple Scattering of Electrons, Phys.Rev. 57 (1940) 24--29.

[25] S. Goudsmit, J. Saunderson, Multiple Scattering of Electrons. II, Phys.Rev. 58 (1940) 36--42.